Efficient photodegradation of Azucryl Red by copper doped TiO2 nanoparticles – Experimental and modelling studies

Ahmed Kerrami
University of Bejaia Laboratory of Materials Technology and Process Engineering: Universite de Bejaia Laboratoire de Technologie des Materiaux et Genie des Procedes
Lotfi Khezami (lkhezami@gmail.com)
Al Imam Mohammad Ibn Saud University https://orcid.org/0000-0001-5747-3114
Mohamed Bououdina
University of Bahrain College of Health Sciences
Laila Mahtout
University of Bejaia Laboratory of Materials Technology and Process Engineering: Universite de Bejaia Laboratoire de Technologie des Materiaux et Genie des Procedes
Abueliz Modwi
Qassim University College of Science and Arts in Alrass
Souhila Rabhi
University of Bejaia Laboratory of Materials Technology and Process Engineering: Universite de Bejaia Laboratoire de Technologie des Materiaux et Genie des Procedes
Faycal Bensouici
Universite M'Hamed Bougara Boumerdes Faculte des Sciences
Hayet Belkacemi
University of Bejaia Laboratory of Materials Technology and Process Engineering: Universite de Bejaia Laboratoire de Technologie des Materiaux et Genie des Procedes

Research Article

Keywords: Sol-gel, Cu-doping, Rutile, Anatase, Phase transformation, Photodegradation, Azucryl red

Posted Date: March 11th, 2021

DOI: https://doi.org/10.21203/rs.3.rs-254332/v1

Efficient photodegradation of Azucryl Red by copper doped TiO_2 nanoparticles – Experimental and modelling studies

Ahmed Kerrami [a], Lotfi Khezami [b, *], Mohamed Bououdina [c], Laila Mahtout [a], Abueliz Modwi [d], Souhila Rabhi [a], Faycal Bensouici [e], Hayet Belkacemi [a]

[a] Materials Technology and Process Engineering Laboratory, University of Bejaia, Algeria.

[b] Department of Chemistry, College of Sciences, Imam Mohammad Ibn Saud Islamic University (IMSIU), P.O. Box 5701, Riyadh 11432, Saudi Arabia.

[c] Department of Physics, College of Science, University of Bahrain, PO Box 32038, Kingdom of Bahrain

[d] Department of Chemistry, College of Science & Arts, Qassim University, Ar Rass Saudi Arabia.

[e] Department of Physics, URMPE Unite, UMBB University, 35000 Boumerdes, Algeria.

* Corresponding author: Lotfi Khezami (lkhezami@gmail.com)

Abstract

This work aims to investigate the effect of copper doping on the photocatalysis performance of TiO_2 nanoparticles for disposal wastewater from organic pollutants. X-ray diffraction analysis manifests the crystallization of a rutile phase for pure and copper-doped TiO_2 except for 2% resulting in a rutile-to-anatase phase transformation. The crystallite size is found less affected by Cu doping; i.e. ~30 nm. BET analysis indicates a decrease in the specific surface area as the doping loading increases. Scanning electron microscopy observations reveal spherical particles at the nanometer range for pure TiO_2 then larger agglomerates of ultrafine particles with Cu doping. FTIR analysis notifies the existence of hydroxyl groups that will promote the photocatalysis process. The photodegradation of Azucryl Red (AR) has been investigated under different conditions; i.e., Cu-loading, initial concentration of AR, and pH. The kinetics of the photodegradation process is further found to comply with the Lagergren kinetic law, regardless the experimental conditions. Nevertheless, the photodegradation process is not only controlled by the intra-particle diffusion mechanism, but also by mass transfer through a liquid film boundary. The maximum degradation of AR, i.e. 86%, has been achieved at pH = 5.0 during 60 minutes of contact time for the 2% Cu-doping, with effective regeneration. The Freundlich model exhibits a better fitting for AR dye photodegradation equilibrium data, compared to Langmuir, Temkin and Dubinin-Radushkevich.

Keywords: Sol-gel; Cu-doping; Rutile; Anatase; Phase transformation; Photodegradation; Azucryl red.

1. Introduction

Industrial activities generate significant volumes of water contaminated by polluting organic and inorganic matter. The organic contaminants include synthetic dyes in the industrial sector that are widely used in the paper industry, cosmetics, food and especially in the textile industry (El Haddad, Regti, Laamari, Mamouni, & Saffaj, 2014; Mahdavinia & Zhalebaghy, 2012; Perez-Urquiza, Prat, & Beltran, 2000). These non-biodegradable dyes are likely to contaminate the environment, besides being responsible for various environmental alterations, especially water resources, their presence in the water, their pollution rate and their problem of water pollution.

Although several techniques have been adopted for organic dyes remediation, the heterogeneous photocatalysis currently appears as a very promising and potential technological alternative. Indeed, during the process of degradation, there will be the destruction of organic pollutants, such as dyes, while leading to a complete mineralization (Fernández-Garcıa et al., 2000; Joshi & Shrivastava, 2011). It has been reported that the photocatalytic process depends mainly on the characteristics of the molecule to be degraded, the light source and the type of semiconductor acting as a photocatalyst (gap and texture). In the literature, the widely investigated photocatalysts are zinc oxide (ZnO) and titanium dioxide (TiO_2) (Hoffmann, Martin, Choi, & Bahnemann, 1995; Kormann, Bahnemann, & Hoffmann, 1988; Liu & Yang, 2003; Pelizzetti, Minero, Piccinini, & Vincenti, 1993; Villaseñor, Reyes, & Pecchi, 1998; William IV, Kostedt, Ismail, & Mazyck, 2008).

Titanium dioxide is currently considered to be the most efficient semiconductor owing to its enhanced photocatalytic performance, non-toxicity, low cost, durability and chemical stability to corrosion (Hoffmann et al., 1995), as well as for its large and tunable bandgap (3.2 eV for anatase and 3.0 eV for rutile). Moreover, it uses UV rays containing only a small part (about 3 to

5%) of solar energy (Linsebigler, Lu, & Yates Jr, 1995). Many efforts have recently been devoted to optimize the characteristics of TiO_2 in the visible (Wu, Dong, Zhao, & Guo, 2008) such as through the doping TiO_2 with transition metal ions (Anpo & Takeuchi, 2003; Chen et al., 2002; Einaga, Harada, Futamura, & Ibusuki, 2003; Thaminimulla, Takata, Hara, Kondo, & Domen, 2000; Xie & Yuan, 2003) and non-metallic anions (Asahi, Morikawa, Ohwaki, Aoki, & Taga, 2001; Burda et al., 2003; Gómez et al., 2003; Yu, Yu, Ho, Jiang, & Zhang, 2002). Moreover, other approaches have been also proposed, such as the coupling with narrow-band semiconductors (Bartl, Boettcher, Frindell, & Stucky, 2005; Bartl, Puls, Tang, Lichtenegger, & Stucky, 2004; Kumar & Jain, 2001) and sensitization with dyes (Viseu, Hungerford, & Ferreira, 2002). Besides, it is well-known that the doping process of TiO_2 by metals and transition metals is much easier than using non-metallic elements (Iwaszuk & Nolan, 2011).

This research work, aims to investigate the influence of Cu as an effective transition metal dopant in order to improve TiO_2 photocatalytic properties (Srinivas et al., 2011). TiO_2 and Cu-doped nanopowders are prepared using the sol-gel method then characterized by XRD, SEM/EDX, BET, and FTIR. The photocatalytic performance of the as-prepared nanopowders is studied using azucryl red (AR) molecule as a textile dye. The photodegradation data were modeled using different kinetics and equilibrium models. A mechanism of the photodegradation process was proposed and discussed.

2. Experimental Part

2.1. Synthesis of Photocatalysts

Pure and Cu-doped TiO_2 powders are prepared via a cost-effective and straightforward procedure. The precursor tetraethyl-orthotitanate ($(C_2H_5O)_4Ti$, Merk 95%) was dissolved in ethanol, water, and nitric acid (HNO_3 Biochem 69%) solution. The mixture was roughly stirred

using a magnetic agitator for one hour. After 24 hours of soaking, the mixture was oven-dried at 100°C and continuously stirred in air. The obtained powder was amorphous. The sol of Cu-doped TiO_2 was prepared using the identical method as previously detailed, with the addition of copper nitrate ($Cu(NO_3)_2$) to the TiO_2 solution. The as-produced powders are subsequently calcinated for one hour at 600°C.

2.2. Characterization of Photocatalysts

The structure of the as-prepared powders was checked by X-ray powder diffraction (XRD) using Rigaku Ultima IV diffractometer with Cu-Kα X-ray source (λ = 1.5418 Å). The morphological examinations have been accomplished by field emission scanning electron microscopy (FESEM) employing LYRA3 TESCAN provided with a dispersive electron X-ray (EDX) spectrometer for the specification of the chemical composition. The BET (The Brunauer, Emmett and Teller) specific surface area (SSA), average pore diameter and volume were determined from nitrogen adsorption-desorption isotherms performed at the boiling point (-195.8°C) of N_2 through an ASAP 2020 (Micromeritics) apparatus. Each sample was outgassed using He for 2h at 250°C to take off moistness and impurities prior to the adsorption experiment. The BET model and t-plot scheme of Lippens and de Boer (Lippens & De Boer, 1965) were used to calculate the porosity and surface area. The FTIR chemical bonding were analyzed using an Nicolet 6700 spectrometer, FTIR spectra were achieved in the interval of 4000–400 cm^{-1} with a resolution of 4 cm^{-1}.

2.3. Photocatalytic Degradation Measurements

The photocatalysis test was carried out at atmospheric pressure and room temperature in a catalytic photoreactor, as described elsewhere (Kerrami et al., 2019). 0.2 mg of catalyst was added

110 to 2 mL of azucryl red (AR) solution having an initial concentration C_0= 1,247x10^{-5} mol.L^{-1} in a
111 quartz container. The heterogeneous mixture was then irradiated with UV light with a cut filter
112 (365 nm) using a UV light lamp (Spot Light Source 300-450nm, L9588-01, Hamamatsu, Japan)
113 and kept under magnetic agitation. The absorbance was measured for different exposure periods
114 of time using a spectrophotometer scan (39919.FEB /10) at a maximum absorption wavelength of
115 about 532 nm.
116 The amount of adsorbed AR dye was calculated according to the formula:

117 $$q_t = \frac{V(C_0 - C_t)}{m} \quad (1)$$

118 where q_t (mg.g^{-1}) is the adsorbed dye amount per gram of adsorbent at time t (min), V is the solution
119 volume (L), C_0 and C_t are the initial concentration and concentration of AR dye (mg.L^{-1}) in solution
120 at any time t, and m the mass of the adsorbent (g).

121 The quantity adsorbed (mg dye/g material) at equilibrium q_e was estimated through an analogue
122 expression:

123 $$q_e = \frac{V(C_0 - C_e)}{m} \quad (2)$$

124 where C_e is the liquid-phase concentrations of AR dye at equilibrium time.

125 **3. Results and Discussion**

126 **3.1 X-ray diffraction analysis**

127 Figure 1 illustrated the evolution of X-ray diffraction patterns of pure and Cu $_{2\text{-}10\%}$ doped
128 TiO_2. Qualitative phase analysis indicates the formation of rutile phase for pure TiO_2, followed by
129 phase transformation into anatase phase for $Cu_{2\%}$, which in turn undergoes a second phase

transformation into original rutile phase for $Cu_{4\%}$ and $Cu_{10\%}$ doped TiO_2. Figure 1 also displays that all diffraction peaks are comparatively broad and intense, implying the formation a nanoscale phase with high crystallinity. For pure TiO_2, the observed peaks at 2θ = 27, 36, 41, 44, 54, 56, 62, 64 and 69° are indexed as (110), (101), (111), (211), (220), (002), (311), (301), and (112) reflections of the tetragonal rutile phase, in conformity with JCPDS card No. JCPDS card No. 01-075-1750. For $Cu_{2\%}$ doped TiO_2, the newly emerged diffraction peaks detected at 2θ = 25.3, 37.8, 48.1, 53.9, 55.1, 62.7, 68.8, 70.4 and 75.07° are indexed as (101), (004), (200), (105), (211), (204), (116), (220), and (215) reflections of the tetragonal TiO_2 (anatase phase) structure in accordance with JCPDS card No. 00-021-1272 (Pongwan, Wetchakun, Phanichphant, & Wetchakun, 2016). Whereas for $Cu_{4\%}$ and $Cu_{10\%}$ doping contents, all the diffractions peaks belong to the tetragonal rutile phase similarly to pure TiO_2. However, it is important to mention that for Cu doping in the range 4–10%, new low intensity diffraction peak appears around of 2θ = 44 ° attributed to the (111) reflection belonging to Cu metal in agreement with JCPDS card No. 02-1225 (Del Carro, 2018).

In a similar work, Park et al. reported that anatase-rutile phase transformation of TiO_2 occurred at 2.5 wt.% Cu doping using low temperature process at 60 °C for 4 and 14 h (Park, Kim, Kim, & Lee, 2006). Besides, due to the differences between the ionic rays (Ti^{4+} = 0.64 Å and Cu^{2+} = 0.73 Å) and the cationic charges of Ti (+4) and Cu (+2), oxygen vacancies may be formed for maintaining charge neutrality (Sahu & Biswas, 2011).

The average crystallite size (D) of Cu $_{x\%}$-doped TiO_2 nanoparticles have been calculated by using the most intense peak (101) anatase and (110) rutile by applying the Scherrer equation:

$$D = \frac{K\lambda}{\beta \cos\theta} \qquad (3)$$

where λ is the X-ray wavelength (1.5417 Å), θ is the Bragg angle, and β is the full width at half maximum of the corresponding peak.

153 According to Williamson–Hall approach (Zak, Majid, Abrishami, & Yousefi, 2011), strain
154 and crystallite size contribute significantly to the diffraction lines broadening (equation 4) (Bindu
155 & Thomas, 2014; Pandiyarajan & Karthikeyan, 2012). In the uniform deformation model (*UDM*),
156 it is assumed that a crystal is isotropic and subsequently its properties are independent of the
157 crystallographic direction along which the measurement is considered.

158 $$\beta_{hkl} \cos \theta_{hkl} = \frac{k\lambda}{D} + 4\varepsilon \sin \theta_{hkl} \quad (4)$$

159 A plot of $\beta_{hkl} \cos \theta_{hkl}$ versus $4 \sin \theta_{hkl}$ represents a linear graph (Ungár, 2007), whereas
160 microstrain (ε) and the crystallite size (D) are calculated from the slope and intercept of the linear
161 plot, respectively.

162 The d-spacing and the lattice parameters have been estimated by following expressions:

163 $$d = \frac{\lambda}{2 \sin \theta} \quad (5)$$

164 $$\frac{1}{d^2} = \frac{h^2 + k^2}{a^2} + \frac{l^2}{c^2} \quad (6)$$

165 All calculated structural (d-spacing and lattice parameters) and microstructural (crystallite
166 size and microstrain) parameters are given in Table 1. The mean crystallite size values estimated
167 using the Scherrer equation and Williamson–Hall model are virtually identical, signifying that the
168 inclusion of strain in the modified formulae of W–H method has inconsequential impact on the
169 average (D) value. Yet, the average crystallite size estimated using Scherrer's and W–H methods
170 exhibit little disparity that can be ascribed to the variation in particle size distribution averaging
171 (Zak et al., 2011). Both values of crystallite size have the same trend, with 4% Cu doping
172 exhibiting the smallest crystallite size of 26 (29) nm and the lowest microstrain with 48×10^{-5} %.

173 The lattice parameters of pure TiO_2 are found to be vary anisotropically compared to the
174 standard values of rutile phase; a and b increase from 4.5912 to 4.5937 while c decreases from

2.9599 to 2.9587 Å without any significant variation in the unit cell volume; i.e. 62.39 compared to 62.43 $Å^3$. Concerning the influence of Cu doping on the lattice parameter, it can be noticed that for 2% Cu loading, the calculated values (a=b=3.7834 Å and c=9.5181 Å) are marginally smaller in contrast to that of the standard pure anatase phase with a tetragonal structure; i.e. a=b=3.7852 Å and c=9.5139 Å (JCPDS card No. 00-021-1272). However, insignificant change in the lattice parameters is observed for the rutile phase, the lattice volume for 4 and 10% Cu-doping is around 62.42 and 62.45 $Å^3$, respectively compared to 62.43 $Å^3$ (a=b=4.5937 Å, c=2.9587 Å; JCPDS card No. 01-075-1750). This can be explained as follow: (i) for smaller loading, Cu^{2+} (0.73 Å) dissolve into TiO_2 host lattice by occupying Ti^{4+} (0.64 Å) sites resulting in lattice contraction/expansion; (ii) however, for charge balance of stoichiometric TiO_2, the compensation of the missing positive charge (+2 for each Cu^{2+} replacing one Ti^{4+}) will be compensated by the creation of oxygen vacancy (-2); (iii) the creation of oxygen vacancy will be accompanied by a contraction of the unit cell. Therefore, the simultaneous occurrence of lattice expansion / contraction results in insignificant change in lattice parameters of TiO_2 upon Cu doping. Moreover, due to relatively large difference in ionic radii (0.64 and 0.73 Å) and charge difference (+4 and +2), a limit of solubility is reached, resulting in the precipitation of Cu metal for higher doping concentrations.

3.2 Morphological observations and chemical analysis

Figure 2 displays the surface particles' morphology of pure and 2% Cu-doped TiO_2 powders have with the corresponding elemental chemical analysis. SEM image of pure TiO_2 powder (Fig. 2a) consists of spherical-shaped particles at the nanoscale with relatively homogeneous size distribution and tendency to agglomeration. Upon 2%Cu doping (Fig. 2b), the powder consists of relatively large agglomerates of ultrafine particles (melted surfaces) with the formation of pores, resulting in improved specific surfaces and consequently very beneficial for

198 the photocatalytic activity. The EDX spectrum of pure TiO_2 indicates the existence of O and Ti
199 elements only, in addition to Cu after doping, signifying the purity of the as-prepared powders.
200 The elemental chemical composition indicates that the Ti/O (24.2 / 50.12 = 0.482) ratio is very
201 close to 0.5, thereby in compliance the stoichiometry of the starting precursor solution. The amount
202 of Cu (1.56 at. %) is also close to the intended content (2.0 at. %), in accordance with the initial
203 precursor solution. The grain size was determined using the imageJ software. The results showed
204 that doping with Cu decreases the particle size; from 29.23 nm fore pure TiO_2 up to 19.58 nm for
205 2% Cu doped TiO_2, which is very beneficial for the photocatalytic reaction.

206 **3.3 FTIR analysis**

207 Figure 3 displays the FTIR spectra of pure and Cu-doped TiO_2 powders. All samples
208 exhibit a broad band setting in the wavenumber range 3250 - 3700 cm^{-1}, which corresponds to the
209 stretching vibrations of the hydroxyl groups of water molecules. The small band at 2350 cm^{-1} for
210 Cu-doped TiO_2 is ascribed to the CO_2 molecule in the atmosphere (Baneshi, Haghighi, Jodeiri,
211 Abdollahifar, & Ajamein, 2014), while the band at 1635 cm^{-1} corresponds to the bending and
212 stretching OH groups adsorbed on the catalyst surface (Baneshi et al., 2014). Surprisingly, such
213 bands are not detected in pure TiO_2 having, signifying that the surface of pure TiO_2 contains fewer
214 hydroxyl groups than Cu-doped TiO_2 which can be attributed to the loss of water during
215 calcination. In the region lower than 1071 cm^{-1}, the absorption bands are assigned to the Ti-O
216 stretching band and O-Ti-O flexural vibration modes (Lopez et al., 2002), which confirm the
217 formation of TiO_2 phase.

218 **3.4 BET Measurements**

219 The isotherm shape provides information on pore size, volume, and distribution as well as
220 whether its macro-, meso-, or micro-porous structure. The nitrogen adsorption-desorption

isotherms are plotted for pure and 2% Cu-doped TiO_2 powders, as illustrated in Figure 4. Both curves display a sorption isotherm of type IV, which is associated with capillary condensation, respectively of nitrogen and argon adsorbed at 77 K and 87 K, occurring in mesoporous solids having cylindrical pores, as well as H1 hysteresis loops according to IUPAC classification (Sotomayor, Cychosz, & Thommes, 2018; Thommes et al., 2015). This kind of isotherm is obtained with mesoporous adsorbents having a pore radius ranging between 25 and 500Å (Thommes et al., 2015). Such a hysteresis loop depicts uniformly arranged spherical or agglomerated nanoparticles (as shown in SEM images Fig. 2), with respective to TiO_2 higher specific surface area and pore volume (Table 2).

Surprisingly, the surface area has been dramatically reduced upon the addition of Cu, even at low content (2%), during the doping process. Systematically, a decrease of the pores' average diameter and volume is observed, ranging from (13-20 nm) to (19-24 nm) and 108 x 10^{-3} up to 4.5 x10^{-3} $cm^3.g^{-1}$, respectively. Maurice et al. (Sorolla II, Dalida, Khemthong, & Grisdanurak, 2012) found a similar effect of Cu-doping when preparing 2 wt% Cu-TiO_2 via the sol-gel route. The decline in the surface characteristics can be explained by the blocking of the pore entrance at the surface of TiO_2 (Sorolla II et al., 2012). However, the appearance of hysteresis loop in the isotherm of Cu-doped nanopowder indicates that the pore blockage does not take place over the entire material.

The BJH method has been used to determine the pore size distribution, as illustrated by the inset graphs in Figure 4. As it can be depicted in Figure 4a, the pore size distribution of pure TiO_2 nanopowder is narrow and ranging between 15 - 30 nm with an average pore diameter of about 23.4 nm. Meanwhile, the pore size distribution of Cu-doped nanopowder is dispersed in a broad interval from 10 to 40 nm with an average pore diameter equal to 19.6 nm (Fig. 4b). As it can be

observed, the incorporation of Cu within TiO_2 host lattice even at such low doping level generated lowering of pore diameter and volume as well as broadening and uniformity of pore size distribution. This finding implies that Cu is well dispersed into TiO_2 network causing some modifications of the mesostructure at its surface, which corroborate with XRD analysis.

3.4. Photodegradation kinetics study of Azucryl red

The study of the photodegradation kinetics and mechanism is very essential in processing aqueous wastewater as it avail precious information on the degradation process. The degradation kinetics has been performed by varying the amount of catalyst, the initial pH of AR solution as well as the initial AR dye concentrations. Equation (6) represents a pseudo-first-order model of Lagergren (Shahwan, 2015; Sorolla II et al., 2012) with a rate constant k_{app} (min^{-1}) and q_e the maximum quantity of AR adsorbed at equilibrium. The plot of C_t/C_0 against t allows the determination of k_{deg}:

$$\frac{C_t}{C_0} = \mathrm{Exp}\left(-k_{deg}.t\right) \qquad (7)$$

The kinetics results of the photodegradation process under UV irradiation are displayed in Figure 5 (a, b, and c). The values of k_{deg} and the linear regression coefficient (r^2) are computed by the simulation of the model using Origin Pro software and are summarized in Tables 3. According to the regression coefficient, mainly greater than 0.96, the experimental results are well simulated by the Lagergren pseudo-first-order model for the tested adsorbents. As can be noted, from Figure 5, photolysis does not affect the degradation of AR; however, the presence of the photocatalyst reduces extremely the concentration of the dye. Based on the obtained rate constants, the half-life time ($t_{1/2} = \ln 2/k_{deg}$) has been also calculated and compared (Shahwan, 2015). As shown in Table 3, the value of $t_{1/2}$ obtained based on the rate constant of Eq. (6) ranges from 18 up to 65 min, which is much closer to the experimental values.

The adsorption of AR on the surface of the catalyst and its photodegradation can be governed by the mass transfer through the boundary liquid film and/or by the intra-particular diffusion/transport process. The linearized equation of mass transfer kinetic model proposed by Ketcha Mbadcam *et al.* (Ho & McKay, 1998) is expressed as follows:

$$\mathrm{Ln}(\mathrm{C_0} - \mathrm{C_t}) = \mathrm{Ln}(\mathrm{D}) + \mathrm{k_0}.\mathrm{t} \qquad (8)$$

where D is the mass transfer constant and k_0 (min^{-1}) the adsorption constant. AR may be carried from the liquid phase to the solid particles by the intra-particle diffusion process. The mass transfer kinetic model constants are obtained from the slope and the intercept of the straight line Ln (C_0 - C_t) *vs.* time. The linear plots illustrated in Figure 6 (a, b, and c) and mass transfer model constants are given in Table 3.

Sometimes, such a mechanism model is a rate-limiting stage in the adsorption or photodegradation process. The probability of intra-particular diffusion is examined through the Weber and Morris diffusion model (Hameed, Salman, & Ahmad, 2009; Mbadcam, Anagho, & Nsami, 2011):

$$q_t = k_{dif}.t^{1/2} + C \qquad (9)$$

where C, the intercept yields more details regarding the thickness of the boundary layer. The intra-particle diffusion constant, k_{dif} value (in $mg.g^{-1}.min^{1/2}$), for the tested adsorbent is obtained from the slope of the graph (Fig. 7 (a, b and c)) as illustrated in Table 3. The validity of these models is thereafter discussed on the basis of the regression coefficient r^2.

3.4.1 Effect of Cu-doping concentration

Figure 5a displays the photocatalytic decomposition of the azucrylic dye in aqueous solution by pure and Cu-doped TiO_2 nanopowders under UV irradiation. As it can see, the azucryl red decays constantly throughout the irradiation time for all nanopowders. The photocatalytic

elimination efficiency of Cu-doped TiO_2 for 2% and 4% reaches approximately 85.26 and 77.64% of the initial concentration after 60 minutes of irradiation, respectively. Whereas beyond this value, the degradation rate decreases, and pure TiO_2 shows only 73.84% of AR elimination efficiency. This indicates that Cu-doping even in small loading, promotes the photocatalytic reaction. Therefore, 2%Cu represents the optimal metal charge for the effectiveness of strengthening the photocatalytic activity of TiO_2.

From Table 3, it can be observed that the highest constant efficiency (K_{deg}) is obtained for 2 and 4% Cu, with 3.83 x 10^{-2} and 2.7510^{-2} min^{-1}, respectively. Then it decreases drastically to 1.16 x 10^{-2} min^{-1} for 10% Cu beneath the obtained value for pure TiO_2. This finding may indicate that a larger content of copper will deteriorate the catalytic photodegradation capacity.

There may be the probable causes for the reduction of the photocatalytic efficiency at high Cu-doping content: (i) the active sites present at the surface of catalyst are covered with an excess of Cu; (ii) the combination of the charge carriers increases the rate photocatalytic degradation with higher amount of Cu charge (Kim et al., 2013; Morikawa, Irokawa, & Ohwaki, 2006).

3.4.2 Effect of initial AR solution pH

The influence of the initial solution pH (i.e., pH = 3.0, 5.0, 6.0, and 8.0 ± 0.1) on the degradation of AR by pure and Cu-doped TiO_2 nanopowders under UV-irradiation, are presented in Figure 5b and the calculated Lagergren model constant values are given in Table 3.

The obtained results show that the azucryl red photodecoloration is higher in the case of acidic pH medium, and the value of K_{deg} constant increases for the pH change from 3.0 to 5.0, subsequently decreases for higher pH value. The most significant degradation kinetics is observed at a pH of 5.0 (Table 3). Besides, the effect of the solution's initial pH on the photodegradation process is

substantial, since it influences the electric charge of the particles. Indeed, in acidic medium, the dye adsorption occurs at the surface of TiO_2 particles, may be due to the electrostatic attraction between the positively charged TiO_2 and the negatively charged dye. However, the rate of photodegradation decreases with increasing pH (pH > 6). In the present study, the azucryl red is deprotonated and negatively charged for the basic pH. The same applies to TiO_2 (Katz, McDonagh, Tijing, & Shon, 2015), and the repulsion between the azucryl red anion and TiO_2 particles decreases the initial velocity of the dye pollutant degradation.

3.4.3 Effect of AR initial concentration

Figure 5c depicts the influence of the initial Azucryl red concentration (5, 10, 15, and 20 mg. L^{-1}) on the photocatalytic degradation process in the presence of 0.2 mg of pure and Cu-doped TiO_2 catalysts. The Lagergren constant and r^2 values are summarized in Table 3. The obtained results prove that the effect of the initial concentration of Azucryl red is inversely proportional to the rate of degradation. Indeed, the higher the concentration of Azucryl red, the longer the degradation time is, until 15%Cu doping concentration. Beyond this value, the effectiveness of AR degradation has increased, which can be explained by the enhancement in the pollutant-surface attraction to the photocatalyst. Thus, for the same period of irradiation, i.e., 60 min, the degradation yield of Azucryl red in solutions of 5 and 10 mg. L^{-1} is found to be 85.2 and 57.55%, respectively.

In contrast, for higher concentration of 15 and 20 mg. L^{-1}, the degradation yield reaches a steady state; i.e. only 45.96 and 46.89%. Several authors reported this phenomenon related to the efficiency of photocatalytic degradation and the decrease in constant velocity with increasing substrate concentration (da Silva & Faria, 2003). This result can be explained by the fact that when

334 the dye concentrated in a solution is high; the phenomenon of diffusion of light by the dye
335 molecules will be essential and will have a negative influence on the degradation activity.

336 The photodegradation of AR at the surface of the tested adsorbents may be controlled by
337 the intra-particle rate model, since, q_t and $t^{1/2}$ convene a linear correlation (Fig. 7 (a, b, and c)).
338 Besides, the regression coefficient values, regardless of the studied conditions, are mostly higher
339 than 0.96, signifying that the data are strictly appropriate to the model. The thickness of the
340 boundary layer is highly matched up with the *C* values. Nevertheless, Figure 7 (a, b, and c), linear
341 curves do not pass across the origin. This annotation can be ascribed to some level of boundary
342 layer control. The mentioned phenomenon is an allusion that the intra-particle diffusion is not the
343 only rate-limiting stage, as supplementary kinetic processes may affect the photodegradation
344 activity. In other words, the as mentioned physic-chemical parameters are intervening concurrently
345 and cannot be neglected (Royer et al., 2009; Yazdani, Tuutijärvi, Bhatnagar, & Vahala, 2016).
346 Meanwhile, this finding can be correlated by the results obtained using mass transfer model,
347 namely, the high values of regression coefficients (Tables 3). Besides, linear relation has been
348 observed (Fig. 6 (a, b, and c)), and the regression coefficients are higher than 0.91, except in the
349 case of Cu-doping concentration 10% and pH 6.2 (0.7966, 0.8324, respectively). This finding
350 points out that the photodegradation kinetic process may also be controlled by mass transfer
351 through a liquid-particle interface, namely, the mass transfer by convection (Royer et al., 2009).

352 **3.5. Photodegradation Equilibrium study of azucryl red**

353 Photodegradation isotherms can represent the equilibrium established between the azucryl
354 red on the adsorbent and the unadsorbed component in the solution. The most widely used isotherm
355 equations for equilibrium data modeling are Langmuir (Langmuir, 1918), Freundlich (Freundlich,

1907), Temkin (Allen, Mckay, & Porter, 2004), and Dubinin-Radushkevich (D-R) (da Silva & Faria, 2003) isotherms and they are expressed as follow:

$$\frac{C_e}{q_e} = \frac{1}{q_m} C_e + \frac{1}{q_m.b} \quad \text{linear form of Langmuir equation} \quad (10)$$

$$Lnq_e = \frac{1}{n} LnC_e + LnK \quad \text{linear form of Freundlich equation} \quad (11)$$

$$q_e = \frac{RT}{B} LnK_T + \frac{RT}{B} LnC_e \quad \text{linear form of Temkin equation} \quad (12)$$

$$Lnq_e = Lnq_m - \beta\varepsilon^2 \quad \text{linear form of D-R equation} \quad (13)$$

$$\text{with } \varepsilon = RTLn\left(1 + \frac{1}{C_e}\right)$$

where q_m is the concentration of sorbed adsorbate at nanoparticle-phase, corresponding to the complete monolayer coverage of adsorption sites (Langmuir, 1918), and b is the Langmuir constant concerning the adsorption free energy. The q_m and b values are evaluated from the Langmuir model linear plot (Eq. 9): the slope is $1/q_m$ and the intercept $1/(q_m.b)$. The Freundlich model's constants, k and n, are determined from the slope and intercept of the plot $\ln(q_e)$ against $\ln(C_e)$ (Eq. 10), respectively. K and n constants may be correlated to the strength of the adsorptive bond and the bond distribution, respectively (Freundlich, 1907). The Temkin's isotherm presumes that the heat of adsorption of all molecules increases linearly with coverage (Allen et al., 2004). The linear form of this isotherm can be given by Eq. (11), where B and K_T are Temkin constants, respectively related to the heat of sorption ($J.mol^{-1}$) and Temkin's isotherm constant ($L.mg^{-1}$). The constants B and K_T are determined from the slope and the intercept of the linear plot of q_e against $\mathrm{Ln}(C_e)$. Dubinin-Radushkevich isotherm expression is represented by the equation (12) (Ayawei, Ekubo, Wankasi, & Dikio, 2015), where ε is Polanyi potential, β is D-R's constant, R is gas constant (8.31 $Jmol^{-1}.k^{-1}$), T is absolute temperature, and $E = (2\beta)^{-0.5}$ is mean adsorption energy.

377 It is well-known that the adsorption isotherms help in describing the degradation process
378 at equilibrium conditions. Figure 8 depicts the photodegradation equilibrium isotherms of AR dye
379 (5, 10, 15, 20, and 25 mg.L^{-1}) by $Cu_{2\%}$-TiO_2 nanopowder for 60 minutes at room temperature and
380 5.0 ± 0.2 pH. Besides, the batch experiments data were modeled by the four previously described
381 isotherm models using the least-squares method. The linearized Langmuir, Freundlich, Temkin
382 and D-R isotherms of AR dye in solutions are plotted. Consequently, the respective model
383 parameters (q_m, b, K, n, B, KT, ε, *and* β) with a correlation coefficient (r^2) are determined by the
384 simulation of the different models by using Origin 8 software and summarized in Table 4.

385 The substantial characteristic of the Langmuir model may be manifested in the expression of
386 equilibrium parameter R_L, which is a constant known as the separation factor (Langmuir, 1918):

387 $$R_L = \frac{1}{1 + b.C_0} \qquad (14)$$

388 where R_L value indicates the adsorption nature as irreversible if $R_L = 0$, favorable if $0 < R_L < 1$,
389 linear if $R_L = 1$ and unfavorable if $R_L > 1$.

390 Taking into account the high values of the regression coefficient (r^2=0.9935) as shown in
391 Table 4, it should be pointed out that the Freundlich model exhibits a better fitting for AR dye
392 photodegradation equilibrium data (Fig. 8 and Table 4). Based on this finding, it can be highlighted
393 that the photodegradation data are better described by Freundlich isotherm compared to the
394 remaining models' isotherms, particularly Langmuir. However, from the obtained results, the
395 maximum monolayer coverage capacity (q_m) from the Langmuir isotherm model has been found
396 to be 120 mg.g^{-1} and R_L is about 0.03, indicating that the equilibrium photodegradation is explicitly
397 more favorable (r^2 = 0.9651).

398

3.6 Photocatalytic degradation mechanism

A plausible mechanism for the photocatalytic degradation of AR dye is illustrated in Fig. 9. By means of illumination of the as-prepared $Cu_{x\%}$–TiO_2 nanocatalysts (NC) with UV-light; the electrons in the valence band (VB) are excited to the conduction bands (CB), consequently an equivalent number of holes are formed in the VB.

By means of radiation, the as-prepared $Cu_{x\%}$–TiO_2 nanocatalysts (NC) with UV-light wavelength greater than or equal to its bandgap, the electrons move from the valence bond (VB) to the conduction band (CB) forming an equivalent number of an oxidizing site (hole h^+) and a reduction site (electron e^-) (Ajmal, Majeed, Malik, Idriss, & Nadeem, 2014). Meanwhile, TiO_2 is a semiconductor with a wide bandgap. Furthermore, the incorporation of Cu^{2+} into the TiO_2 matrix will produce intermediate energy levels that occasionally retard in the charge carrier's recombination and, consequently, reinforce the photocatalytic efficiency. The latter process is the oxidation-reduction reaction of the adsorbed reagents on the NC particle surface (Ajmal et al., 2014), the charges arriving at the photocatalyst surface react with the adsorbed substances that can accept or donate electrons. The electrons react with oxygen to yield the superoxide radicals (Kaur & Singhal, 2014), which may interact with the cations H+ to form the radical hydro-peroxide HO_2: (i) and the formation of hydrogen peroxide that decomposes $HO^{\bullet}$ hydroxide radical (ii) to the catalyst surface after excitation by lengths appropriate wave. The h^+ holes react with the reagents adsorbed on the NC surface liable to give electrons such as water, adsorbed OH^- anions or directly organic pollutants (AR), producing highly oxidizing hydroxyl radicals which can oxidize the organic molecules adsorbed on TiO_2 surface until complete mineralization into CO_2 and H_2O as shown in Figure 9.

3.7 Regeneration of the adsorbent

The reusability of photocatalysts nanocomposite is required for their feasible utilization on a large scale for industrial applications. The procedure used to remove dyes molecules from wastewater systems is considered upon numerous criteria like cost, efficiency, and reusability. The recycling of adsorbents and the renewal of adsorbate is a cost-effective process. In this context, the regeneration of the 2% Cu-doped TiO_2 nanoparticles from the dye mixture has been investigated for five cycles. After the photodegradation process, the nanocatalyst was only thoroughly washed with deionized hot water and oven-dried at 100 °C for three hours. The measurements are realized similarly to the photodegradation kinetics and equilibrium process, i.e., pH = 5.0 during 60 minutes of contact time. The adsorption–desorption process has been repeated up to five cycles to test the reusability of the nanoparticles for AR dye molecules degradation. As depicted in Fig. 10, 2% Cu-doped TiO_2 nano-photocatalyst indiscernibly displays a higher degree of stability, and its efficiency is found to be relatively significant for AR dye after five sequential cycles. It is also important to highlight that 2% Cu-TiO_2 nanoparticles fabricated via an amended sol-gel method can be recovered effectively for the reuse in photodegradation for more than five cycles.

4. Conclusion

TiO_2 and Cu-TiO_2 nanopowders were synthesized, characterized, and tested as catalysts in the azucryl red dye's photodegradation. XRD data indicated a rutile-anatase phase transformation for 2% Cu doping, while the crystallite size was slightly affected by Cu loading (around 30 nm). The morphology of the nanoparticles has transformed from spherical-shaped into agglomerated large nanoparticles upon Cu doping. The BET analysis revealed a sudden drop in surface area from 16.5 $m^2.g^{-1}$ for TiO_2 to about 1.0 $m^2.g^{-1}$ after 2% Cu-doping content addition. Photocatalytic

efficiency up to 86 % was achieved at 2% Cu-doping content, at 25°C and a pH of 5.0. The kinetics study of the dye photodegradation process was proved to obey the Lagergren first-order law, regardless of experimental conditions (i.e., %Cu doping concentration, pH, and initial dye concentration). The kinetic investigation indicated that the rate is not only controlled by the intra-particle diffusion process, particularly at its initial phase. Instead, it was proved that this process might also be controlled by mass transfer through the liquid phase's boundary layer. Besides, the Freundlich isotherm yielded a better fitting of the equilibrium data of the photodegradation process. Apart from being highly reusable, the photocatalyst showed excellent performance at a low Cu concentration Cu also. The as-obtained findings on Cu-doped TiO_2 nanopowder demonstrated it as a potential nanocatalyst contender for organic dyes photodegradation.

Authors' contributions:

Ahmed Kerrami: validation, investigation, visualization, resources, writing –original draft, writing - review & editing.

Lotfi Khezami: methodology, validation, writing –original draft, writing - review & editing.

validation, investigation.

Mohamed Bououdina: conceptualization, validation, writing –original draft, writing - review & editing, visualization, supervision.

Laila Mahtout: conceptualization, methodology, resources, supervision.

Abueliz Modwi: methodology, validation, investigation, review & editing.

Souhila Rabhi: validation, investigation, review & editing.

Faycal Bensouici, Hayet Belkacemi: conceptualization, methodology, resources, supervision.

Funding: not applicable.

Data availability: The datasets used and/or analyzed during the current study are available from the corresponding author on reasonable request.

Compliance with ethical standards:

Ethics approval and consent to participate: Not applicable.

Consent for publication: Not applicable.

Competing interest: The authors declare that they have no competing interest

References

Ajmal, A., Majeed, I., Malik, R. N., Idriss, H., & Nadeem, M. A. (2014). Principles and mechanisms of photocatalytic dye degradation on TiO 2 based photocatalysts: a comparative overview. *RSC Advances, 4*(70), 37003-37026.

Allen, S., Mckay, G., & Porter, J. F. (2004). Adsorption isotherm models for basic dye adsorption by peat in single and binary component systems. *Journal of colloid and interface science, 280*(2), 322-333.

Anpo, M., & Takeuchi, M. (2003). The design and development of highly reactive titanium oxide photocatalysts operating under visible light irradiation. *Journal of Catalysis, 216*(1-2), 505-516.

Asahi, R., Morikawa, T., Ohwaki, T., Aoki, K., & Taga, Y. (2001). Visible-light photocatalysis in nitrogen-doped titanium oxides. *Science, 293*(5528), 269-271.

Ayawei, N., Ekubo, A. T., Wankasi, D., & Dikio, E. D. (2015). Adsorption of congo red by Ni/Al-CO3: equilibrium, thermodynamic and kinetic studies. *Oriental Journal of Chemistry, 31*(3), 1307.

Baneshi, J., Haghighi, M., Jodeiri, N., Abdollahifar, M., & Ajamein, H. (2014). Homogeneous precipitation synthesis of CuO–ZrO2–CeO2–Al2O3 nanocatalyst used in hydrogen production via methanol steam reforming for fuel cell applications. *Energy Conversion and management, 87*, 928-937.

Bartl, M. H., Boettcher, S. W., Frindell, K. L., & Stucky, G. D. (2005). 3-D molecular assembly of function in titania-based composite material systems. *Accounts of chemical research, 38*(4), 263-271.

Bartl, M. H., Puls, S. P., Tang, J., Lichtenegger, H. C., & Stucky, G. D. (2004). Cubic mesoporous frameworks with a mixed semiconductor nanocrystalline wall structure and enhanced sensitivity to visible light. *Angewandte Chemie International Edition, 43*(23), 3037-3040.

Bindu, P., & Thomas, S. (2014). Estimation of lattice strain in ZnO nanoparticles: X-ray peak profile analysis. *Journal of Theoretical and Applied Physics, 8*(4), 123-134.

Burda, C., Lou, Y., Chen, X., Samia, A. C., Stout, J., & Gole, J. L. (2003). Enhanced nitrogen doping in TiO2 nanoparticles. *Nano letters, 3*(8), 1049-1051.

Chen, C., Li, X., Ma, W., Zhao, J., Hidaka, H., & Serpone, N. (2002). Effect of transition metal ions on the TiO2-assisted photodegradation of dyes under visible irradiation: a probe for the interfacial electron transfer process and reaction mechanism. *The Journal of Physical Chemistry B, 106*(2), 318-324.

da Silva, C. G., & Faria, J. L. (2003). Photochemical and photocatalytic degradation of an azo dye in aqueous solution by UV irradiation. *Journal of Photochemistry and Photobiology A: Chemistry, 155*(1-3), 133-143.

Del Carro, L. (2018). *Sintering of copper nanoparticle pastes for microelectronic packaging.* ETH Zurich,
Einaga, H., Harada, M., Futamura, S., & Ibusuki, T. (2003). Generation of active sites for CO photooxidation on TiO2 by platinum deposition. *The Journal of Physical Chemistry B, 107*(35), 9290-9297.
El Haddad, M., Regti, A., Laamari, M. R., Mamouni, R., & Saffaj, N. (2014). Use of Fenton reagent as advanced oxidative process for removing textile dyes from aqueous solutions. *J Mater Environ Sci, 5*(3), 667-674.
Fernández-Garcıa, M., Martınez-Arias, A., Iglesias-Juez, A., Belver, C., Hungrıa, A., Conesa, J., & Soria, J. (2000). Structural characteristics and redox behavior of CeO2–ZrO2/Al2O3 supports. *Journal of Catalysis, 194*(2), 385-392.
Freundlich, H. (1907). Über die adsorption in lösungen. *Zeitschrift für physikalische Chemie, 57*(1), 385-470.
Gómez, R., López, T., Ortiz-Islas, E., Navarrete, J., Sánchez, E., Tzompanztzi, F., & Bokhimi, X. (2003). Effect of sulfation on the photoactivity of TiO2 sol–gel derived catalysts. *Journal of molecular catalysis A: Chemical, 193*(1-2), 217-226.
Hameed, B., Salman, J., & Ahmad, A. (2009). Adsorption isotherm and kinetic modeling of 2, 4-D pesticide on activated carbon derived from date stones. *Journal of hazardous materials, 163*(1), 121-126.
Ho, Y.-S., & McKay, G. (1998). Sorption of dye from aqueous solution by peat. *Chemical Engineering Journal, 70*(2), 115-124.
Hoffmann, M. R., Martin, S. T., Choi, W., & Bahnemann, D. W. (1995). Environmental applications of semiconductor photocatalysis. *Chemical reviews, 95*(1), 69-96.
Iwaszuk, A., & Nolan, M. (2011). Charge compensation in trivalent cation doped bulk rutile TiO2. *Journal of Physics: Condensed Matter, 23*(33), 334207.
Joshi, K., & Shrivastava, V. (2011). Degradation of alizarine red-S (A textiles dye) by photocatalysis using ZnO and TiO2 as photocatalyst. *Int. J. Environ. Sci, 2*(1), 8-21.
Katz, A., McDonagh, A., Tijing, L., & Shon, H. K. (2015). Fouling and inactivation of titanium dioxide-based photocatalytic systems. *Critical Reviews in Environmental Science and Technology, 45*(17), 1880-1915.
Kaur, J., & Singhal, S. (2014). Facile synthesis of ZnO and transition metal doped ZnO nanoparticles for the photocatalytic degradation of Methyl Orange. *Ceramics International, 40*(5), 7417-7424.
Kerrami, A., Mahtout, L., Bensouici, F., Bououdina, M., Rabhi, S., Sakher, E., & Belkacemi, H. (2019). Synergistic effect of Rutile-Anatase Fe-doped TiO2 as efficient nanocatalyst for the degradation of Azucryl Red. *Materials Research Express, 6*(8), 0850f0855.
Kim, C.-S., Shin, J.-W., Cho, Y.-H., Jang, H.-D., Byun, H.-S., & Kim, T.-O. (2013). Synthesis and characterization of Cu/N-doped mesoporous TiO2 visible light photocatalysts. *Applied Catalysis A: General, 455*, 211-218.
Kormann, C., Bahnemann, D. W., & Hoffmann, M. R. (1988). Photocatalytic production of hydrogen peroxides and organic peroxides in aqueous suspensions of titanium dioxide, zinc oxide, and desert sand. *Environmental science & technology, 22*(7), 798-806.
Kumar, A., & Jain, A. K. (2001). Photophysics and photochemistry of colloidal CdS–TiO2 coupled semiconductors—photocatalytic oxidation of indole. *Journal of molecular catalysis A: Chemical, 165*(1-2), 265-273.
Langmuir, I. (1918). The adsorption of gases on plane surfaces of glass, mica and platinum. *Journal of the American Chemical Society, 40*(9), 1361-1403.
Linsebigler, A. L., Lu, G., & Yates Jr, J. T. (1995). Photocatalysis on TiO2 surfaces: principles, mechanisms, and selected results. *Chemical reviews, 95*(3), 735-758.

554 Lippens, B. C., & De Boer, J. (1965). Studies on pore systems in catalysts: V. The t method. *Journal of*
555 *Catalysis, 4*(3), 319-323.
556 Liu, H.-L., & Yang, T. C.-K. (2003). Photocatalytic inactivation of Escherichia coli and Lactobacillus
557 helveticus by ZnO and TiO2 activated with ultraviolet light. *Process biochemistry, 39*(4), 475-481.
558 Lopez, T., Moreno, J., Gomez, R., Bokhimi, X., Wang, J., Yee-Madeira, H., . . . Reyes, P. (2002).
559 Characterization of iron-doped titania sol–gel materials. *Journal of Materials Chemistry, 12*(3),
560 714-718.
561 Mahdavinia, G. R., & Zhalebaghy, R. (2012). Removal kinetic of cationic dye using poly (sodium acrylate)-
562 carrageenan/Na-montmorillonite nanocomposite superabsorbents. *Journal of Materials and*
563 *Environmental Science, 3*(5), 895-906.
564 Mbadcam, J. K., Anagho, S. G., & Nsami, J. N. (2011). Kinetic and equilibrium studies of the adsorption of
565 lead (II) ions from aqueous solution onto two Cameroon clays: Kaolinite and smectite. *Journal of*
566 *Environmental Chemistry and Ecotoxicology, 3*(11), 290-297.
567 Morikawa, T., Irokawa, Y., & Ohwaki, T. (2006). Enhanced photocatalytic activity of TiO2− xNx loaded
568 with copper ions under visible light irradiation. *Applied Catalysis A: General, 314*(1), 123-127.
569 Pandiyarajan, T., & Karthikeyan, B. (2012). Cr doping induced structural, phonon and excitonic
570 properties of ZnO nanoparticles. *Journal of Nanoparticle Research, 14*(1), 647.
571 Park, H. S., Kim, D. H., Kim, S. J., & Lee, K. S. (2006). The photocatalytic activity of 2.5 wt% Cu-doped TiO2
572 nano powders synthesized by mechanical alloying. *Journal of Alloys and Compounds, 415*(1-2),
573 51-55.
574 Pelizzetti, E., Minero, C., Piccinini, P., & Vincenti, M. (1993). Phototransformations of nitrogen containing
575 organic compounds over irradiated semiconductor metal oxides: Nitrobenzene and atrazine
576 over TiO2 and ZnO. *Coordination Chemistry Reviews, 125*(1-2), 183-193.
577 Perez-Urquiza, M., Prat, M., & Beltran, J. (2000). Determination of sulphonated dyes in water by ion-
578 interaction high-performance liquid chromatography. *Journal of Chromatography A, 871*(1-2),
579 227-234.
580 Pongwan, P., Wetchakun, K., Phanichphant, S., & Wetchakun, N. (2016). Enhancement of visible-light
581 photocatalytic activity of Cu-doped TiO 2 nanoparticles. *Research on Chemical Intermediates,*
582 *42*(4), 2815-2830.
583 Royer, B., Cardoso, N. F., Lima, E. C., Vaghetti, J. C., Simon, N. M., Calvete, T., & Veses, R. C. (2009).
584 Applications of Brazilian pine-fruit shell in natural and carbonized forms as adsorbents to
585 removal of methylene blue from aqueous solutions—Kinetic and equilibrium study. *Journal of*
586 *hazardous materials, 164*(2-3), 1213-1222.
587 Sahu, M., & Biswas, P. (2011). Single-step processing of copper-doped titania nanomaterials in a flame
588 aerosol reactor. *Nanoscale Research Letters, 6*(1), 1-14.
589 Shahwan, T. (2015). Lagergren equation: Can maximum loading of sorption replace equilibrium loading?
590 *Chemical Engineering Research and Design, 96*, 172-176.
591 Sorolla II, M. G., Dalida, M. L., Khemthong, P., & Grisdanurak, N. (2012). Photocatalytic degradation of
592 paraquat using nano-sized Cu-TiO2/SBA-15 under UV and visible light. *Journal of Environmental*
593 *Sciences, 24*(6), 1125-1132.
594 Sotomayor, F. J., Cychosz, K. A., & Thommes, M. (2018). Characterization of micro/mesoporous
595 materials by physisorption: concepts and case studies. *Acc. Mater. Surf. Res, 3*(2), 34-50.
596 Srinivas, B., Shubhamangala, B., Lalitha, K., Anil Kumar Reddy, P., Durga Kumari, V., Subrahmanyam, M.,
597 & De, B. R. (2011). Photocatalytic reduction of CO2 over Cu-TiO2/Molecular sieve 5A composite.
598 *Photochemistry and photobiology, 87*(5), 995-1001.
599 Thaminimulla, C., Takata, T., Hara, M., Kondo, J., & Domen, K. (2000). Effect of chromium addition for
600 photocatalytic overall water splitting on Ni–K2La2Ti3O10. *Journal of Catalysis, 196*(2), 362-365.

Thommes, M., Kaneko, K., Neimark, A. V., Olivier, J. P., Rodriguez-Reinoso, F., Rouquerol, J., & Sing, K. S. (2015). Physisorption of gases, with special reference to the evaluation of surface area and pore size distribution (IUPAC Technical Report). *Pure and Applied Chemistry, 87*(9-10), 1051-1069.

Ungár, T. (2007). Characterization of nanocrystalline materials by X-ray line profile analysis. *Journal of Materials science, 42*(5), 1584-1593.

Villaseñor, J., Reyes, P., & Pecchi, G. (1998). Photodegradation of pentachlorophenol on ZnO. *Journal of Chemical Technology & Biotechnology: International Research in Process, Environmental AND Clean Technology, 72*(2), 105-110.

Viseu, T. M., Hungerford, G., & Ferreira, M. I. C. (2002). Optical and photophysical studies on porphyrin doped TiO2 matrixes. *The Journal of Physical Chemistry B, 106*(8), 1853-1861.

William IV, L., Kostedt, I., Ismail, A. A., & Mazyck, D. W. (2008). Impact of heat treatment and composition of ZnO− TiO2 nanoparticles for photocatalytic oxidation of an azo dye. *Industrial & Engineering Chemistry Research, 47*(5), 1483-1487.

Wu, Z., Dong, F., Zhao, W., & Guo, S. (2008). Visible light induced electron transfer process over nitrogen doped TiO2 nanocrystals prepared by oxidation of titanium nitride. *Journal of hazardous materials, 157*(1), 57-63.

Xie, Y., & Yuan, C. (2003). Visible-light responsive cerium ion modified titania sol and nanocrystallites for X-3B dye photodegradation. *Applied Catalysis B: Environmental, 46*(2), 251-259.

Yazdani, M. R., Tuutijärvi, T., Bhatnagar, A., & Vahala, R. (2016). Adsorptive removal of arsenic (V) from aqueous phase by feldspars: Kinetics, mechanism, and thermodynamic aspects of adsorption. *Journal of Molecular Liquids, 214*, 149-156.

Yu, J. C., Yu, J., Ho, W., Jiang, Z., & Zhang, L. (2002). Effects of F-doping on the photocatalytic activity and microstructures of nanocrystalline TiO2 powders. *Chemistry of Materials, 14*(9), 3808-3816.

Zak, A. K., Majid, W. A., Abrishami, M. E., & Yousefi, R. (2011). X-ray analysis of ZnO nanoparticles by Williamson–Hall and size–strain plot methods. *Solid State Sciences, 13*(1), 251-256.

635 **Figure Captions**

636 **Fig. 1** X-ray diffraction patterns of copper-doped TiO_2 nanopowders.

637 **Fig. 2** SEM images with corresponding EDS spectra of (a) pure TiO_2, and (b) 2% Cu-doped TiO_2

638 nanopowders.

639 **Fig. 3** Infrared spectra of undoped and Cu-doped TiO_2 nanopowders.

640 **Fig. 4** N_2 adsorption-desorption Isotherm of (a) pure TiO_2, (b) 2%Cu-TiO_2 nanopowders and

641 inset figures are BJH pore size distribution of pure TiO_2, 2%Cu-TiO_2 catalysts.

642 **Fig. 5** Kinetics UV photocatalytic degradation at different conditions of **(a)** Cu-doping loading;

643 **(b)** concentration initial pH, and (c) initial concentration of AR.

644 **Fig. 6 (a)** Mass transfer model plots for the photodegradation of 0.5 $mg.L^{-1}$ AR by $Cu_{x\%}$-TiO_2

645 nanopowder at pH 5.0; **(b)** Mass transfer model plots for the photodegradation of AR by $Cu_{2\%}$-

646 TiO_2 nanopowder at different solution initial pH; **(c)** Mass transfer model plots for the

647 photodegradation of different initial doses of AR by $Cu_{2\%}$-TiO_2 nanopowder at pH 5.0.

648 **Fig. 7 (a)** Intra-particle diffusion plots for photodegradation of 0.5 $mg.L^{-1}$ AR by $Cu_{x\%}$-TiO_2

649 nanopowder at pH 5.0; **(b)** Intra-particle diffusion plots for photodegradation of AR by $Cu_{2\%}$-

650 TiO_2 nanopowder at different solution initial pH; **(c)** Intra-particle diffusion plots for

651 photodegradation of different initial doses of AR by $Cu_{2\%}$-TiO_2 nanopowder at pH 5.0.

652 **Fig. 8** photodegradation isotherm models for AR dye by Cu-doped TiO_2 nanopowders using

653 batch mode procedure at 25◦C, adsorbent mass of 0.2 mg; pH fixed at 5.0; and using a contact

654 time of 60 min. Comparison of isotherm models non-linear plot.

655 **Fig. 9** Schematic AR photodegradation over Cu-doped TiO_2 nanocatalysts.

656 **Fig. 10** Reusability of 2% Cu-doped TiO_2 photocatalyst for five successive cycles for the

657 degradation of AR.

Table captions

Table 1. Structural and microstructural parameters of pure and 2% Cu-doped TiO_2 nanopowders as obtained from XRD analysis.

Table 2. BET characteristics of pure and 2% Cu-doped TiO_2 nanopowders.

Table 3. Intraparticle diffusion, mass transfer, and Lagergren pseudo-first-order models' constants for the photodegradation of AR by pure and Cu-doped TiO_2 nanopowders at different conditions.

Table 4. Different equilibrium model isotherm constants for AR photodegradation by 2% Cu-doped TiO_2 nanopowder [m = 0.2mg, pH = 5.0, T = 25^{o}C].

Figures

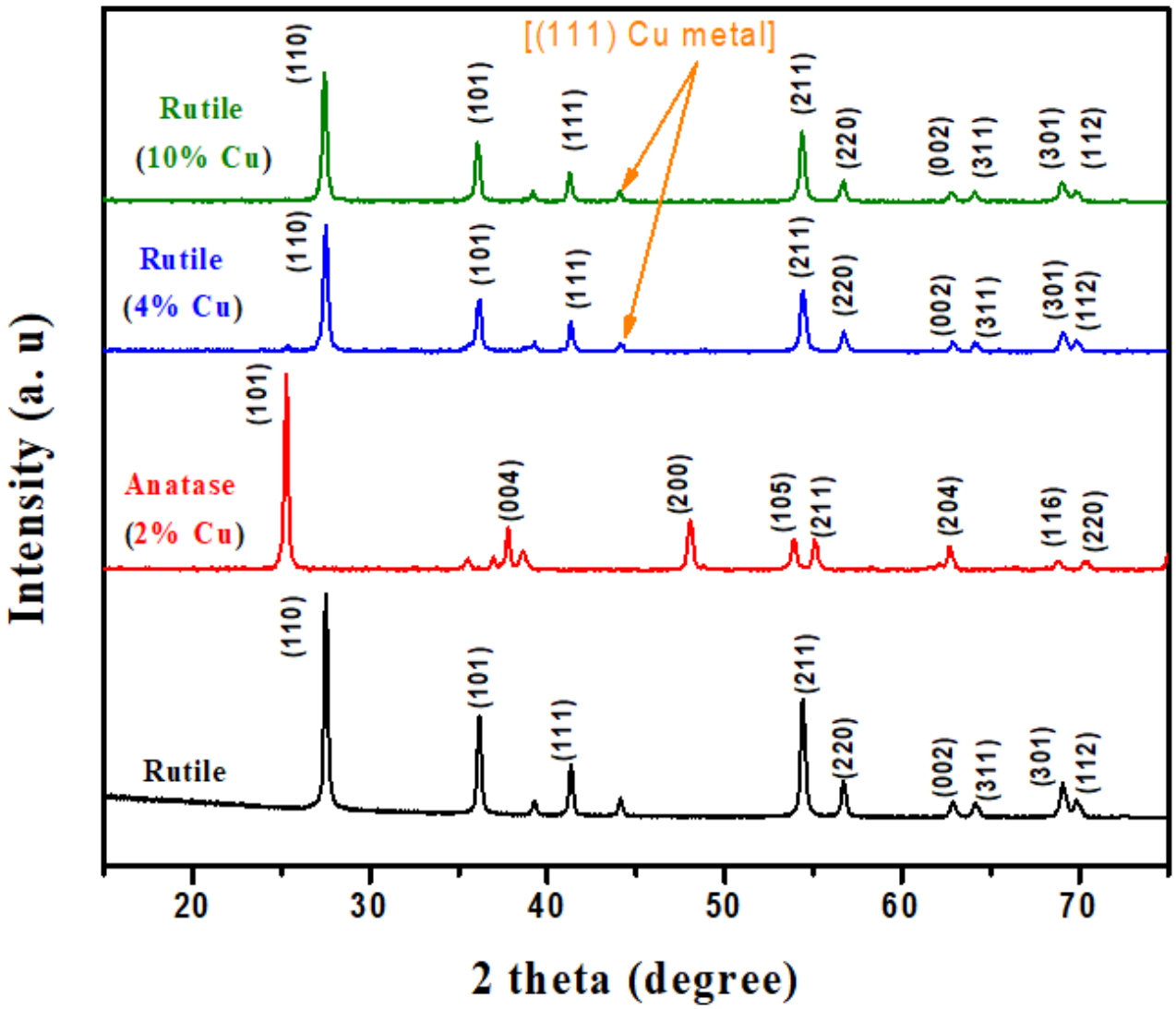

Figure 1

X-ray diffraction patterns of copper-doped TiO2 nanopowders.

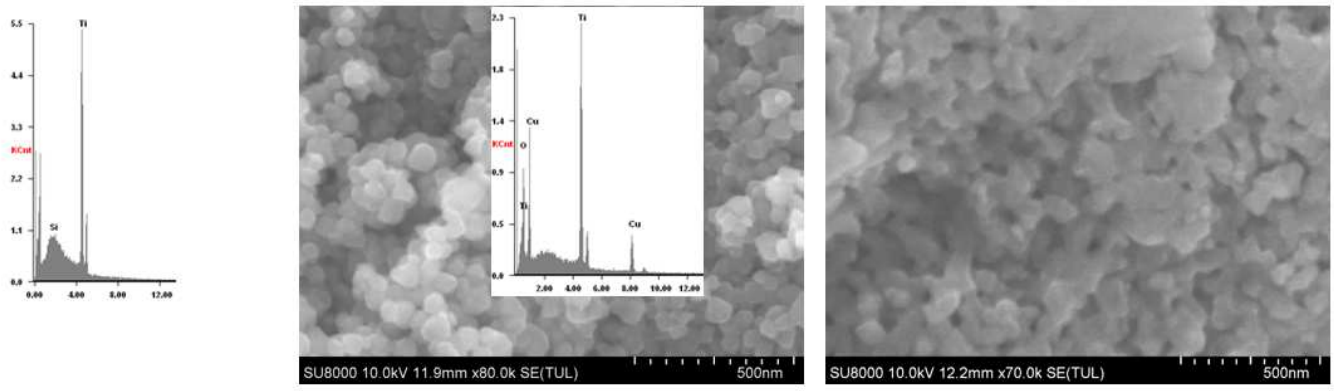

Figure 2

SEM images with corresponding EDS spectra of (a) pure TiO2, and (b) 2% Cu-doped TiO2 nanopowders.

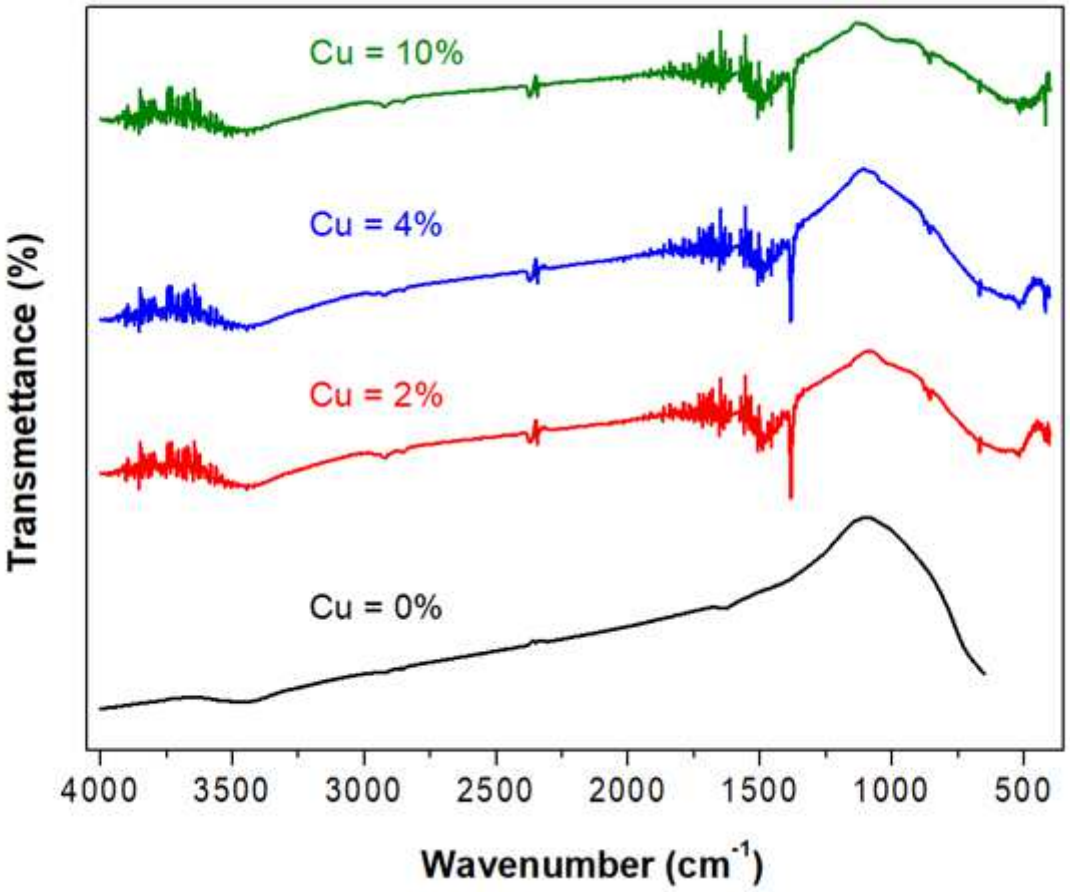

Figure 3

Infrared spectra of undoped and Cu-doped TiO2 nanopowders.

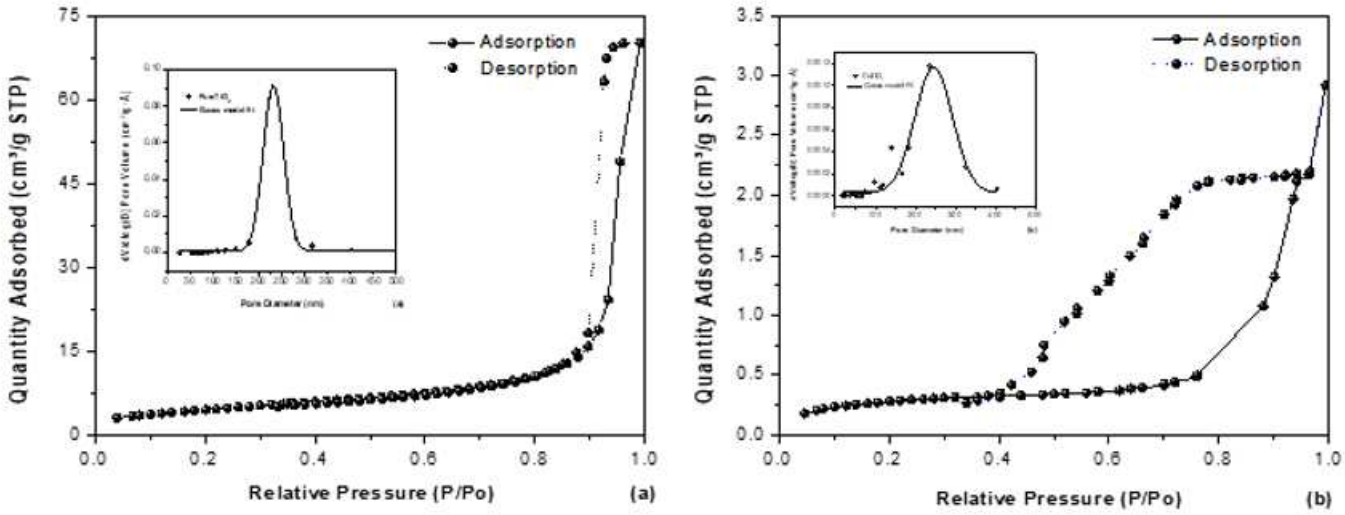

Figure 4

N2 adsorption-desorption Isotherm of (a) pure TiO2, (b) 2% Cu-TiO2 nanopowders and inset figures are BJH pore size distribution of pure TiO2, 2% Cu-TiO2 catalysts.

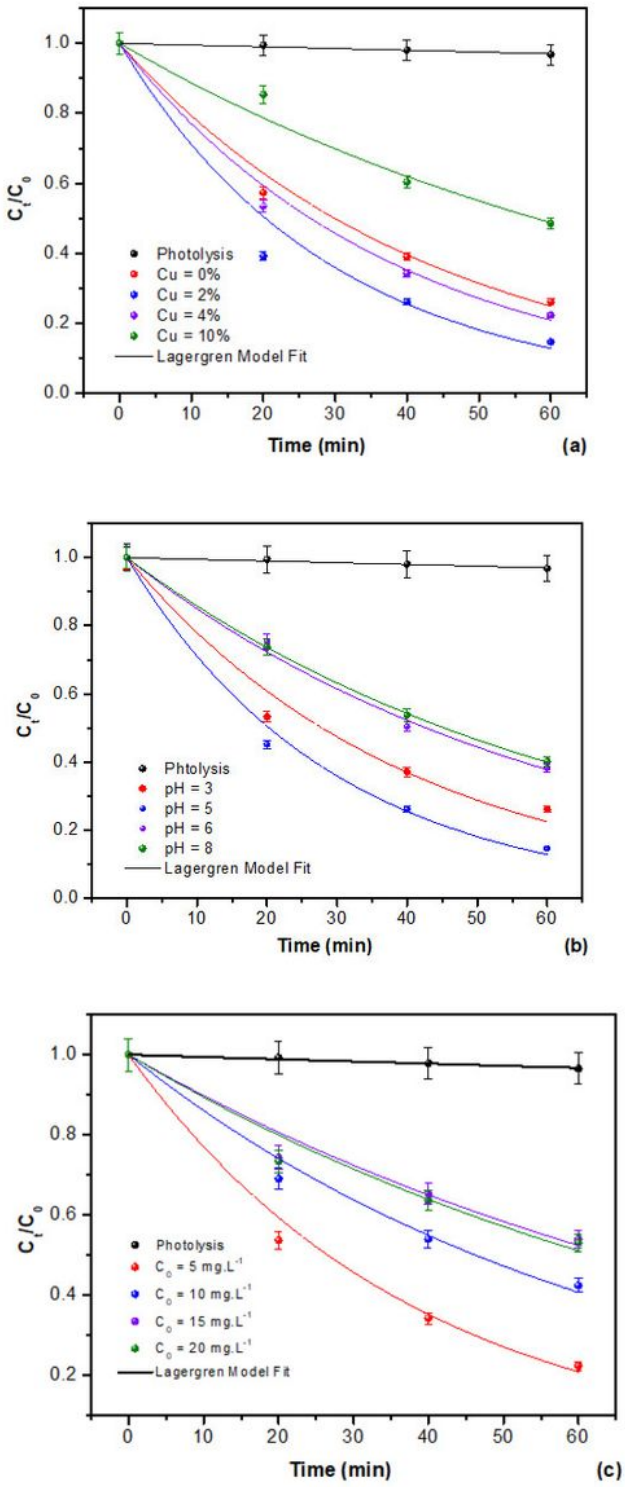

Figure 5

Kinetics UV photocatalytic degradation at different conditions, of (a) Cu-doping loading, (b) concentration initial pH, and (c) initial concentration of Ar

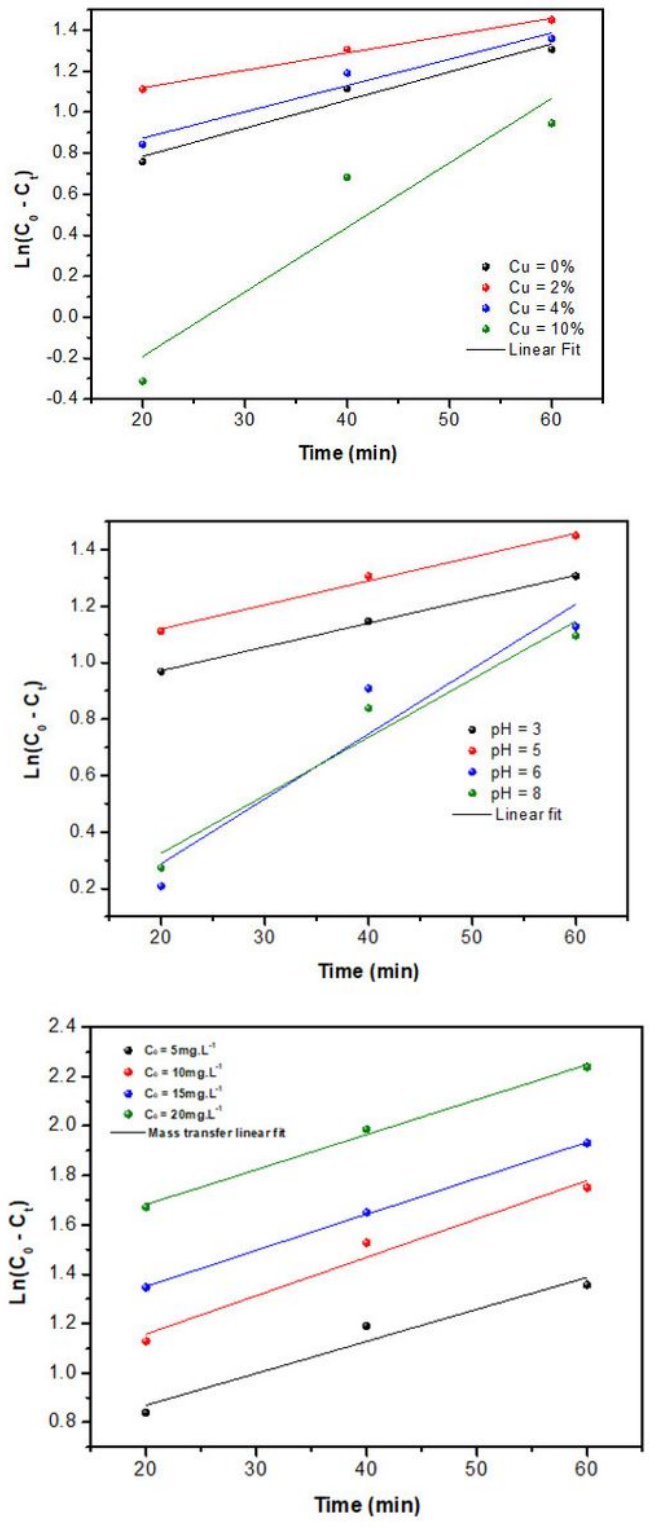

Figure 6

Top panel-a Mass transfer model plots for the photodegradation of 0.5 mg.L-1 AR by Cux%-TiO2 nanopowder at pH 5.0. Middle panel-b Mass transfer model plots for the photodegradation of AR by Cu2%-TiO2 nanopowder at different solution initial pH. Bottom panel-c Mass transfer model plots for the photodegradation of different initial doses of AR by Cu2%-TiO2 nanopowder at pH 5.2

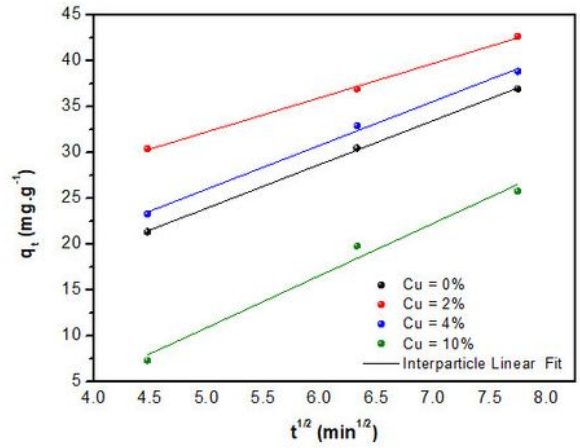

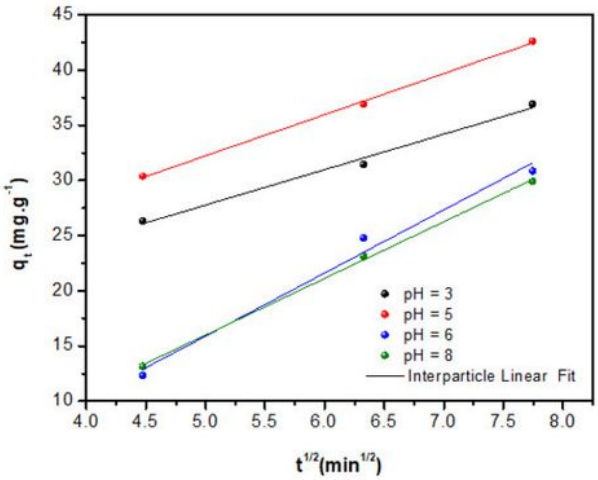

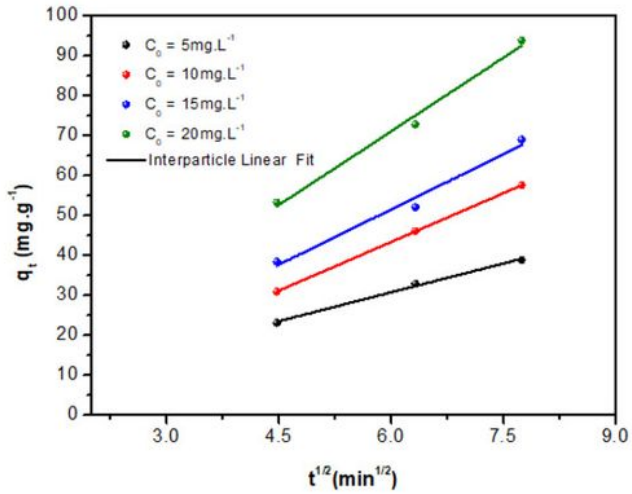

Figure 7

Top panel-a Intra-particle diffusion plots for photodegradation of 0.5 mg.L-1 AR by Cux%-TiO2 nanopowder at pH 5.0. Middle panel-b Intra-particle diffusion plots for photodegradation of AR by Cu2%-TiO2 nanopowder at different solution initial pH. Bottom panel-c Intra-particle diffusion plots for photodegradation of different initial doses of AR by Cu2%-TiO2 nanopowder at pH 5.0.

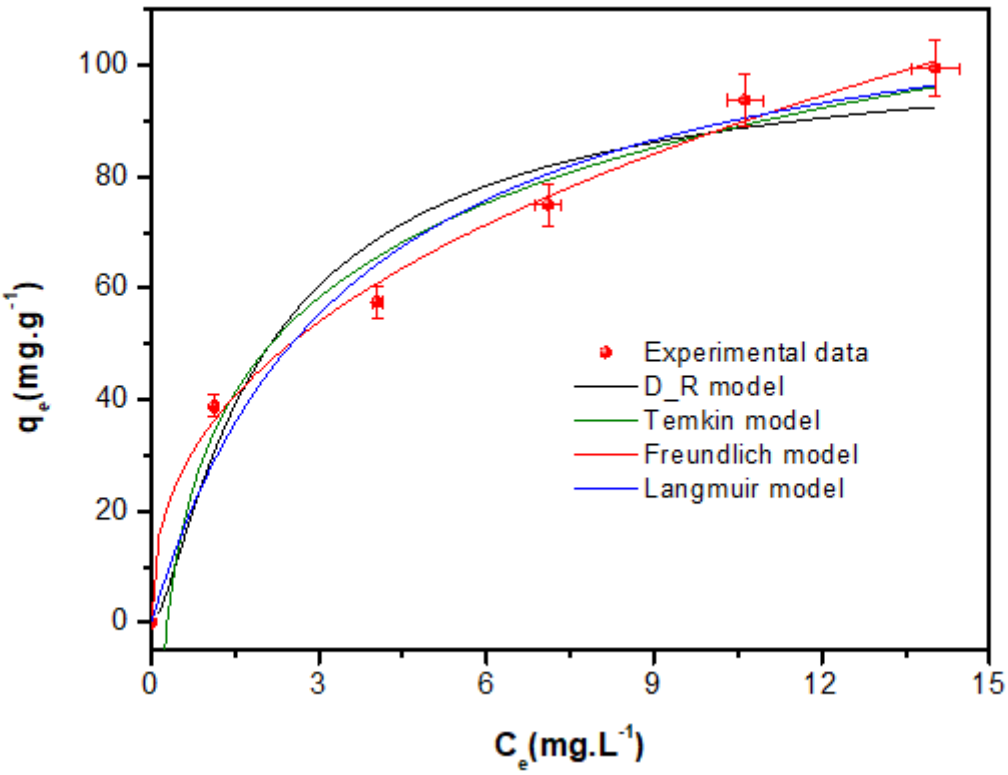

Figure 8

Photodegradation isotherm models for AR dye by Cu-doped TiO2 nanopowders using batch mode procedure at 25□C, adsorbent mass of 0.2 mg; pH fixed at 5.0; and using a contact time of 60 min. Comparison of isotherm models non-linear plot.

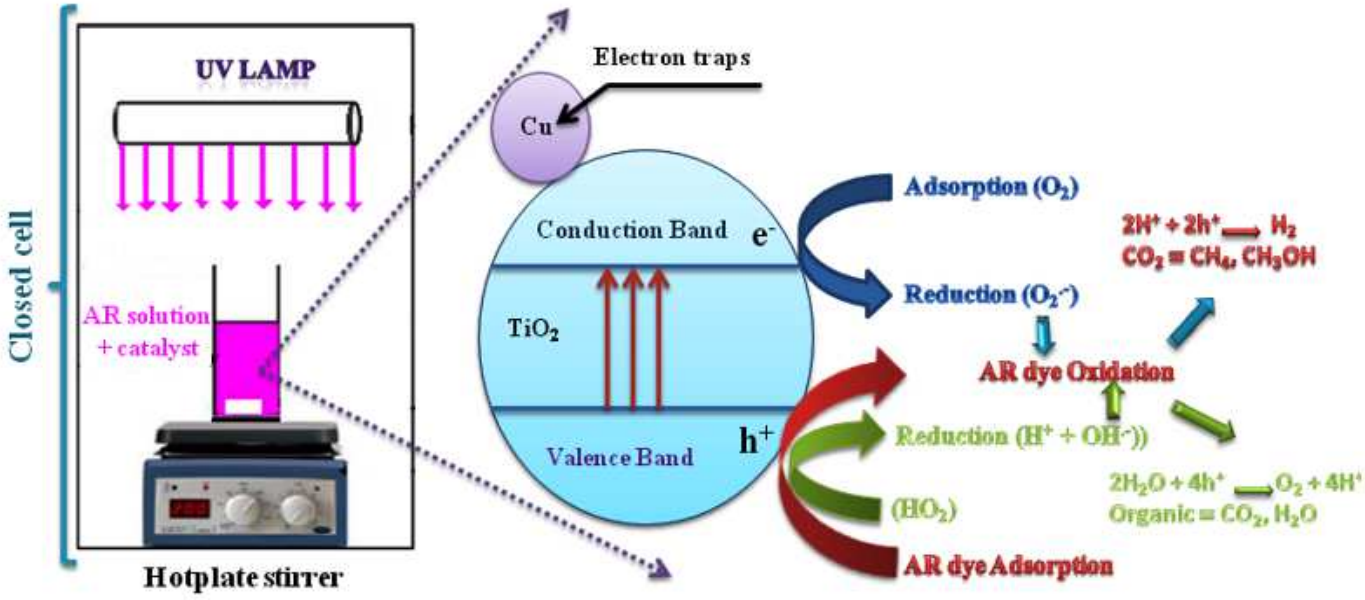

Figure 9

Schematic AR photodegradation over Cu-doped TiO2 nanocatalysts.

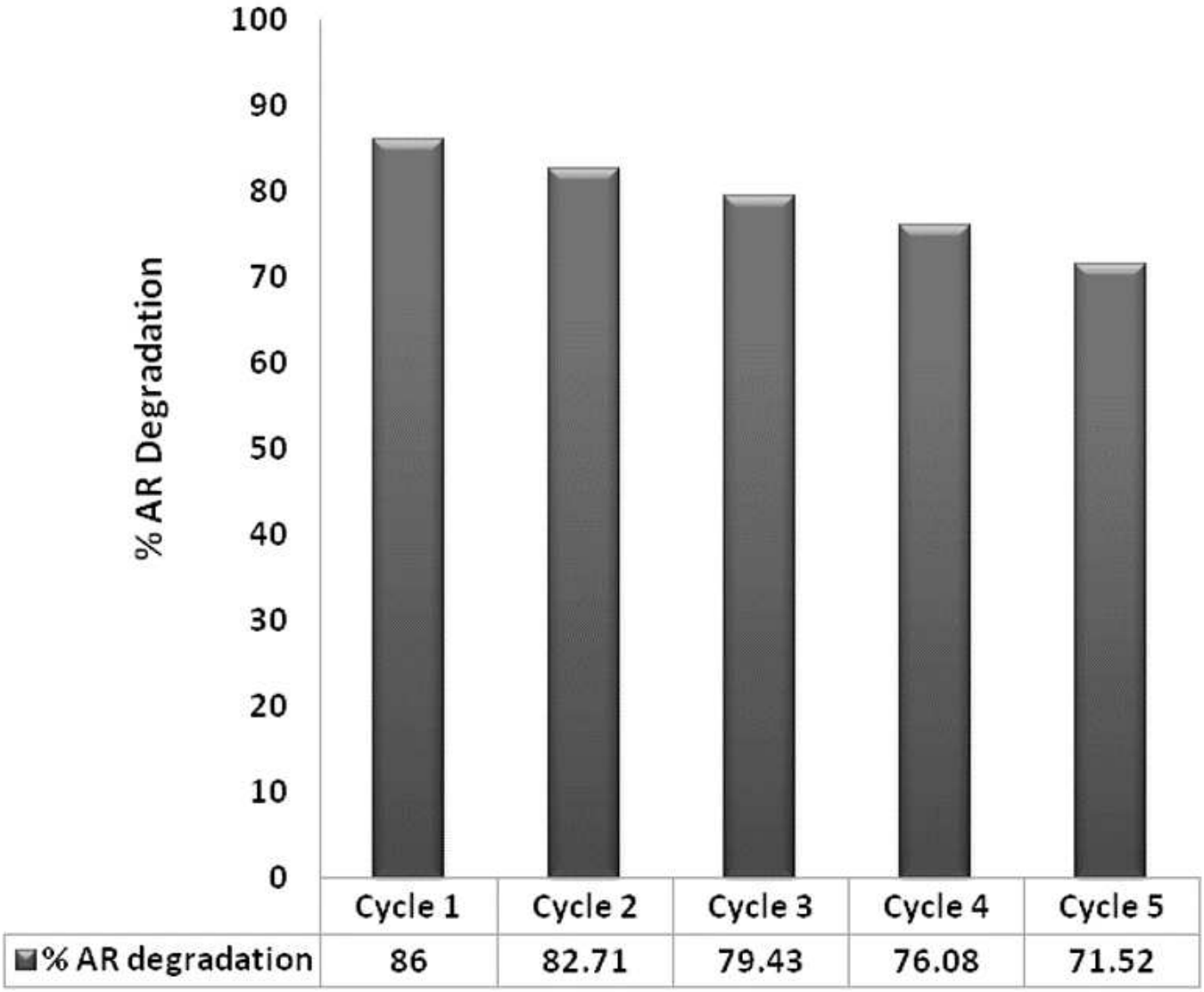

Figure 10

Reusability of 2% Cu-doped TiO2 photocatalyst for five successive cycles for the degradation of AR.